High quality factor silicon-on-lithium niobate metasurfaces for electro-optically reconfigurable wavefront shaping: supplemental document

Elissa Klopfer,[*,†,‖] Sahil Dagli,[†,‖] David R. Barton III,[‡] Mark Lawrence,[*,¶] and Jennifer A. Dionne[*,†,§]

†Department of Materials Science and Engineering, Stanford University, Stanford, California 94305, USA

‡John A. Paulson School of Engineering and Applied Sciences, Harvard University, Cambridge, Massachusetts 02139, USA

¶Department of Electrical and Systems Engineering, Washington University in St. Louis, St. Louis, Missouri 63130, USA

§Department of Radiology, Stanford University, Stanford, California 94305, USA

‖These authors contributed equally to this work

E-mail: eklopfer@stanford.edu; markl@wustl.edu; jdionne@stanford.edu

Origin of the guided mode resonance

We leverage high quality factor guided mode resonances to achieve the phase tunability in our metasurface antennas. The Si layer in our metasurface antenna is capable of supporting guided modes, and can be thought of as a waveguide. The calculated dispersion of a Si waveguide is shown in Fig. S1 as the blue curve. Adding periodic perturbations in the form of notches imposes a Bloch condition on the dispersion curve, folding it at the edge of the first

Brillouin zone (dashed line) such that it intersects the y-axis at a specific wavelength, shown as the cyan curve. The notches provide free space, normally incident light the momentum required to excite this guided mode resonance at the wavelength indicated by the black star.
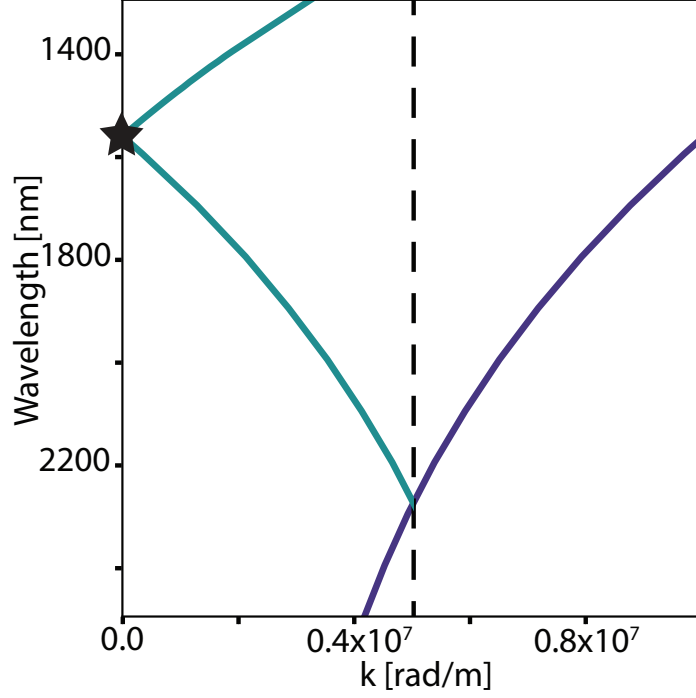

Figure 1: Waveguide dispersion of unnotched bar (blue) and notched bar (cyan).

Using the reflecting metal plate to expand phase modulation range

To construct linear phase gradients in our metasurface, a phase modulation range spanning 2π is desired. We simulate the transmitted and reflected spectra for a metasurfaces without metal reflecting layer (transmitted) and with reflecting layer (reflected), shown in Fig. 2a and b, respectively. Across the resonance in transmission, the phase response spans a range of π. Across the resonance in reflection, the phase response spans a range of 2π. This extra π of range in reflection is a result of the π phase shift from light reflecting off the metal

layer. This expanded phase range allows us to construct phase gradients that span the range required to realize beamsteering and beamsplitting, as demonstrated in the main text, as well as maintains the potential for more complex phase gradients necessary for lensing and beyond.
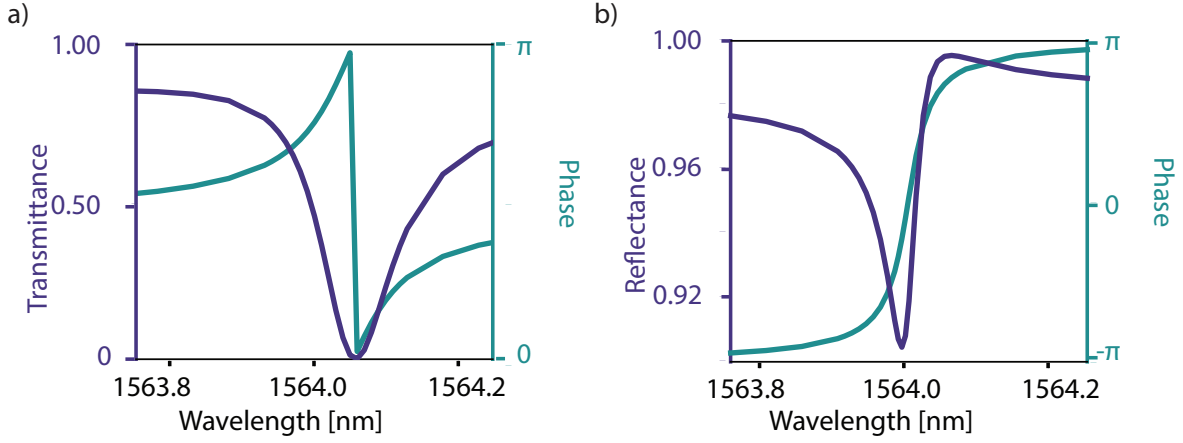

Figure 2: (a) Transmittance and phase response across the resonance in a metasurface without a metal reflecting layer and (b) reflectance and phase response across the resonance in a metasurface with a metal reflecting layer separated from the metasurface by a 610 nm SiO_2 layer.

The Fabry-Perot behavior of light passing through the SiO_2 layer affects the guided mode resonance. In Fig. S3, we calculate the absorption across the resonance with varying metal layer depths below the bottom ground transparent conducting oxide contact. We observe that the linewidth of the resonance, and thus the Q factor, and absorption are both variable to the metal plate depth. As such, the SiO_2 thickness is optimized to balance achieving a high-Q resonance that can be modulated with a reasonable applied voltage range while keeping absorption low to maximize the diffracted efficiency.
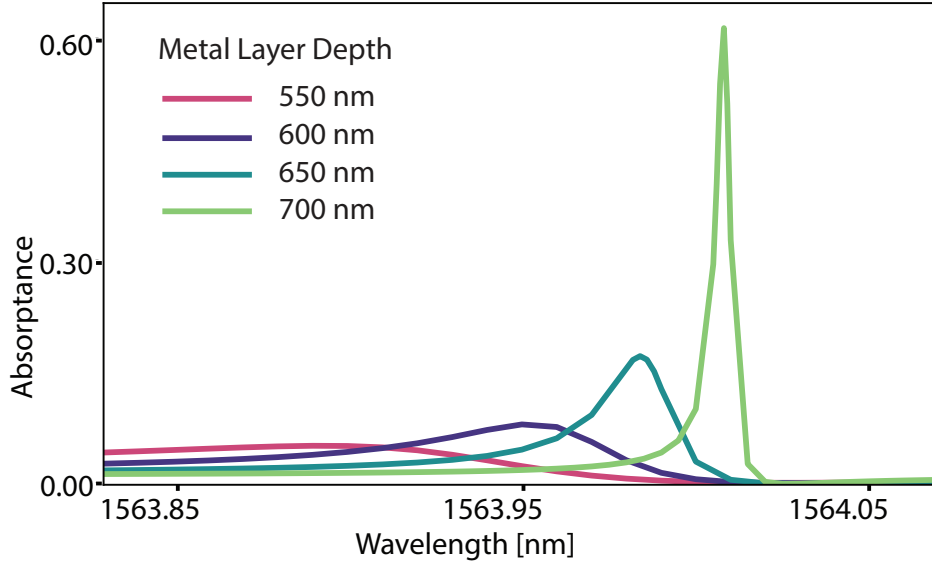
Figure 3: Absorptance across the resonance with varying metal plate depths

Fins for optical and electronic isolation

Arraying resonant nanoantennas with subwavelength spacing can result in crosstalk between neighboring antennas and loss of their individual addressability through coupling. To suppress this coupling and ensure the high-Q modes operate independently from one another while maintaining subwavelength separation, we include a series of "nanofins" between each nanobar. The nanofins are 100 nm wide with a 100 nm center-to-center space between them, so that they act as an effective anisotropic medium to prevent the horizontal high-Q optical modes from coupling to modes in neighboring nanobars.

Figure S4 plots the near field on resonance with two voltages applied for a metasurface (a) without fins and (b) with fins. The metasurface without fins shows near fields with nearly identical magnitudes in neighboring bars. This is due to the the highly resonant bars couple together when no fins are included, and are therefore not able to be individually tuned. By contrast the metasurface with fins shows resonances with varying magnitude in neighboring bars indicating significant and independent shifts in the resonance due to the applied voltage. A similar effect is seen in Figure S5, when three voltages are applied (a) without fins vs (b)

with fins, as well for the case when (c) four or (d) five voltages are applied. This optical isolation we get from our fins is critical for individual addressability between neighboring high-Q bars while maintaining subwavelength separation.
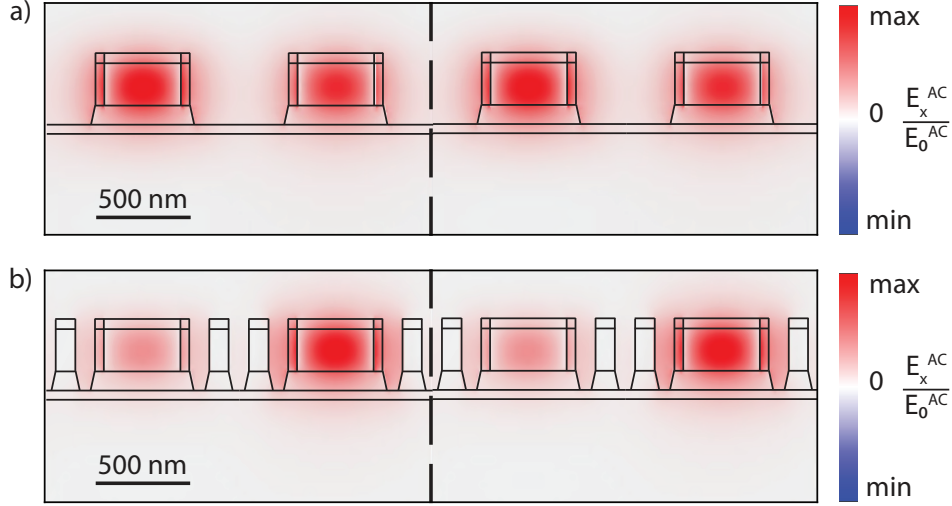

Figure 4: Near field plots for a metasurface on resonance with two voltages applied (a) without fins and (b) with fins.

In addition to the fins improving individual addressability of neighboring antennas by reducing coupling, they also reduce the amount of voltage leaking to neighboring bars significantly. Fig. S6 (a) shows the DC electric field as a function of voltage for one bar, while Fig. S6 (b) shows the DC electric field in a directly adjacent bar in which no voltage is applied as a function of voltage applied to the original bar. When fins are included, the voltage in the first bar results in a much lower DC field in the neighboring bar than in a metasurface without fins. This demonstrates that the fins are crucial for both optical and electronic isolation.

a)

$\dfrac{E_x{}^{AC}}{E_0{}^{AC}}$

500 nm

b)

$\dfrac{E_x{}^{AC}}{E_0{}^{AC}}$

500 nm

c)

$\dfrac{E_x{}^{AC}}{E_0{}^{AC}}$

500 nm

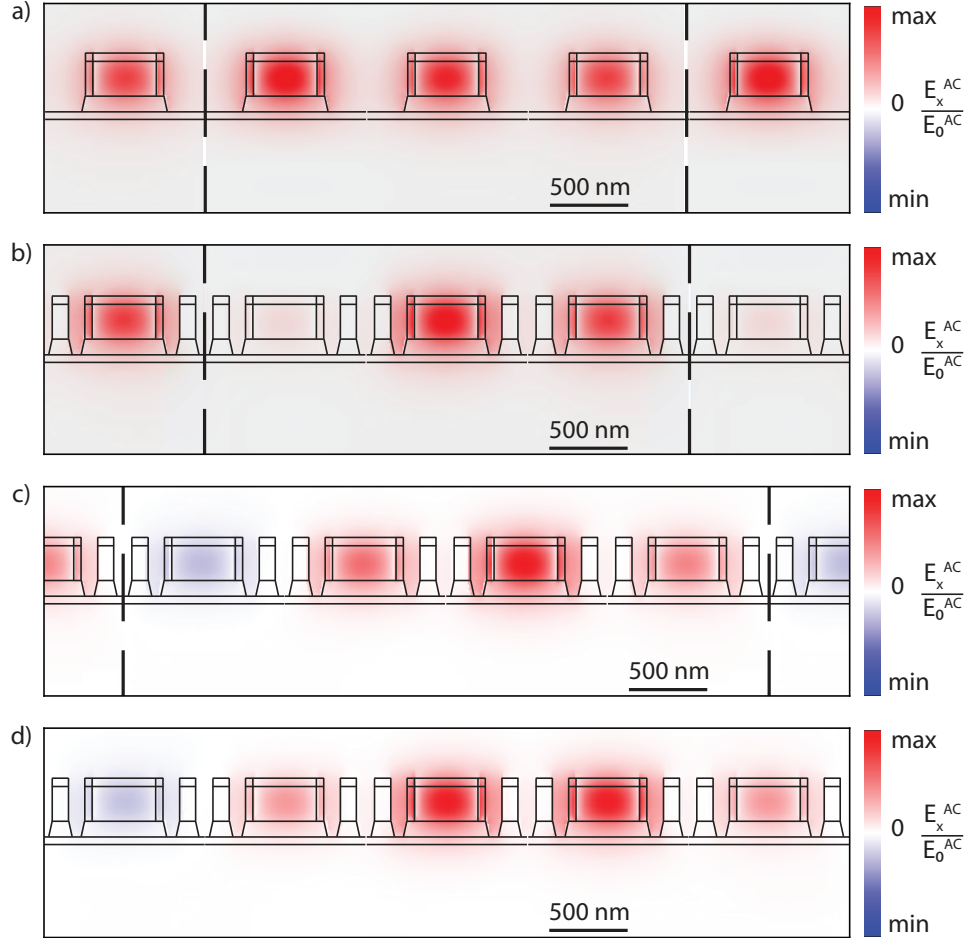d)

$\dfrac{E_x{}^{AC}}{E_0{}^{AC}}$

500 nm

Figure 5: Near field plots for a metasurface on resonance (a) with no fins and three voltages applied, and with fins with (b) three, (c) four, and (d) five voltages applied.
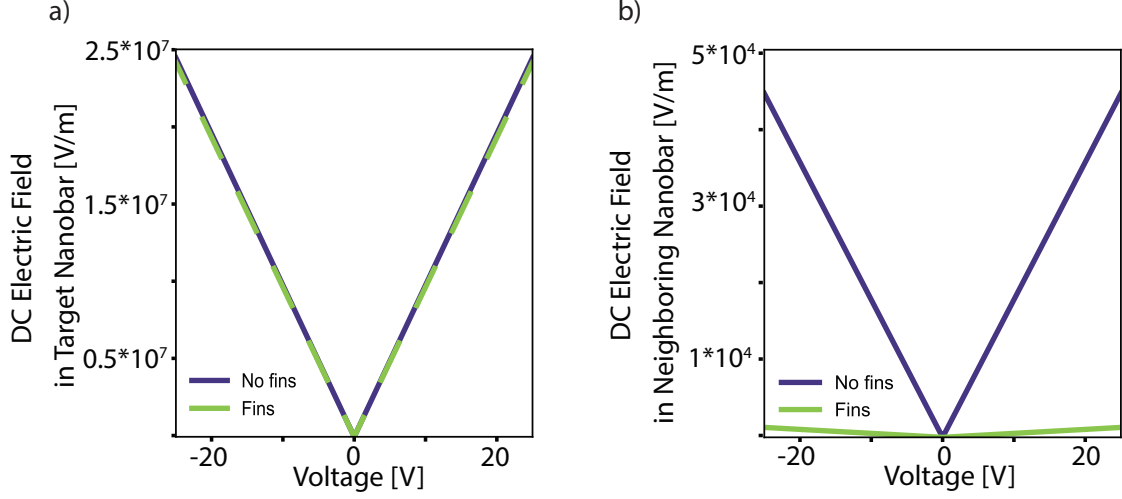
Figure 6: Applied DC electric field in (a) a constituent nanobar in the metasurface and (b) the resulting electric field in a neighboring bar with no applied voltage in a metasurface with and without isolating fins

Orientation of the lithium niobate (LNO) crystallographic axis

Lithium niobate (LNO) is a birefringent material, and LNO thin films are commercially available as x-cut, where the optical axis of the crystal is in the plane of the film, and z-cut, where the optical axis is oriented orthogonal to the film surface. In figure S7a and b, we simulate the reflectance with applied voltage at 1563.96 nm and phase response, respectively, to compare the two options. The full resonance is swept through with less applied voltage for x-cut LNO, resulting in a slightly larger phase modulation range with lower voltage. As such, we chose to use x-cut LNO for our design rather than z-cut.
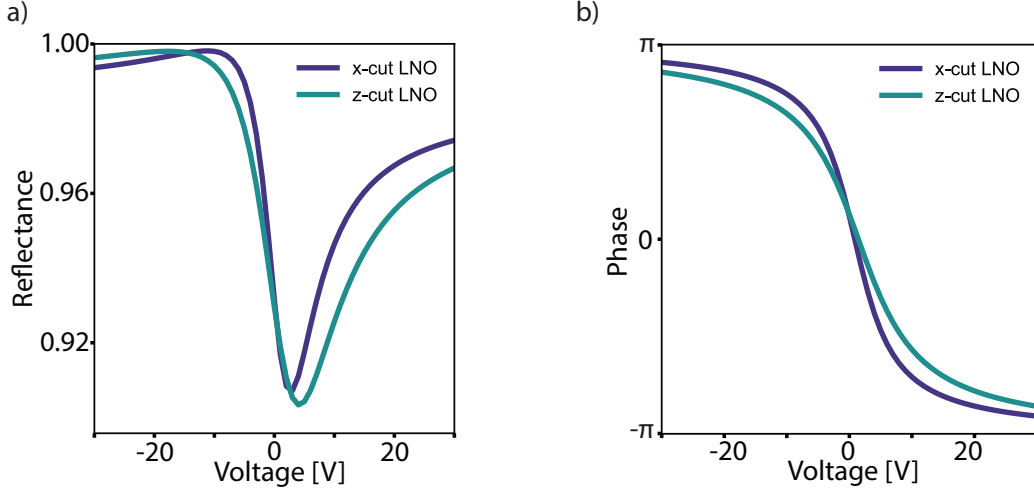
Figure 7: (a) Reflectance and (b) phase response across the resonance with metasurfaces using x-cut and z-cut LNO

Tunable beamsplitting and beamsteering metasurfaces without accounting for residual coupling

If we assume that coupling between neighboring bars is negligible, we can use the phase response from one antenna in an infinitely periodic metasurface to design linear phase gradients. We can achieve beamsplitting and beamsteering using this idealized principle, however it results in lower efficiency devices than the platform is otherwise capable of.

First, we demonstrate beamsplitting by considering a supercell of 2 bars (fig. S8a). Applying voltages of $\pm$ 4.7 V generates a π phase shift between neighboring bars (fig. S8b), which results in a combined $\pm$ 1st diffraction order efficiency of 40%. We then show how our metasurface can form a tunable beamsteerer by modifying the biasing and supercell period of our device. For example, we can use supercells composed of 3 (fig. S9a), 4 (fig. S10a), or 5 (fig. S11a) nanoantennas to dynamically change the steering angle. Using equation 1 in the main text, these correspond to beamsteering angles of 31°, 23°, and 18°, respectfully. To do so, we choose voltages applied to individual bars within the supercell that introduce the desired linear phase variation for each beamsteering angle (figs. S9b, S10b, and S11b). This

corresponds to a difference in phase response between neighboring antennas of $2\pi/3$, $2\pi/4$, and $2\pi/5$ for the 3, 4, and 5 bar supercells respectively. Figs. S9c, S10c, and S11c show the calculated reflection into each potential diffraction order, showing high efficiency at the design wavelength (λ=1563.96 nm). Specifically, we demonstrate beamsteering efficiencies of approximately 60%, 70%, and 80%, respectively, as shown by the preferential diffraction to the +1st order. This demonstrates how constructing phase gradients using the idealized phase response variation found via a uniform voltage applied across the metasurface can still result in beamsteering with efficiencies greater than 50%.
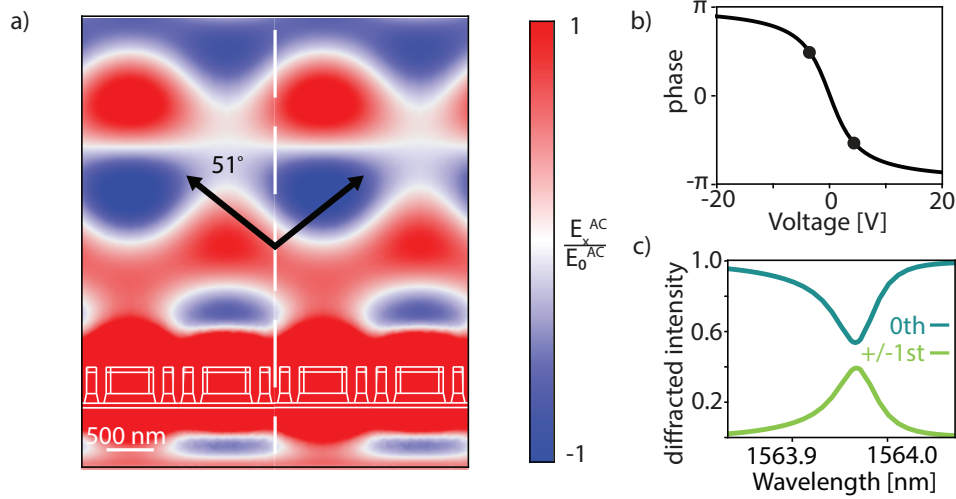

Figure 8: Electro-optically reconfigurable metasurface beamsplitter. (a) Visualization of beamsplitting when the series of two voltages are applied to the metasurface; white dotted lines denote the supercell period. (b) Phase delay dictated by applied voltage without accounting for residual coupling between bars, two voltages (-4.7, +4.7 V) are selected (black markers) to achieve a π phase change between them. (c) Variation in diffraction efficiency into the $\pm$ 1st diffraction order at and away from the resonant wavelength. On resonance the device operates with a combined $\pm$1st order efficiency of 40%.
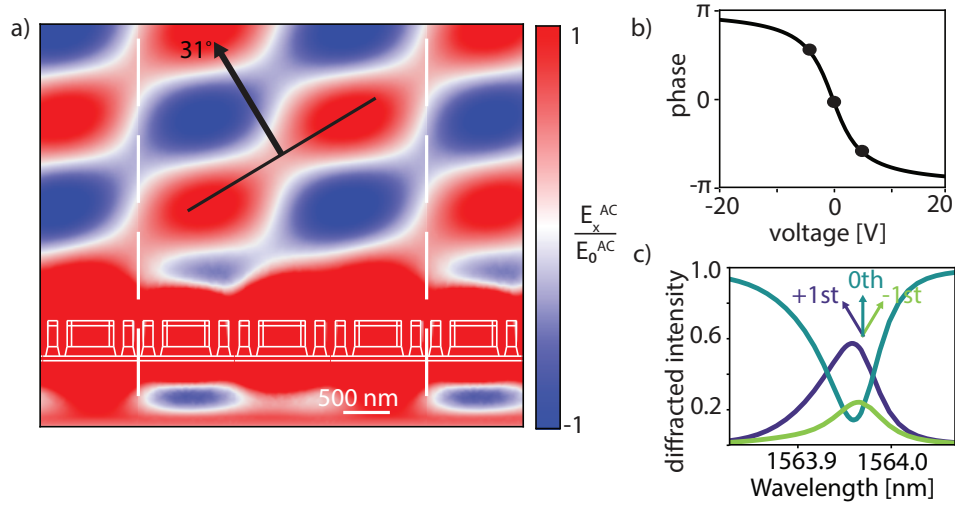
Figure 9: Electro-optically reconfigurable metasurface beamsteerer with three bars in the supercell. (a) Visualization of beamsteering at 1563.96 nm when the series of three voltages are applied to the metasurface; white dotted lines denote the supercell period. (b) Phase delay dictated by applied voltage without accounting for residual coupling between bars, three voltages (-8.1, 0, +8.1 V) are selected (black markers) to achieve a $2\pi/3$ phase change between them. (c) Variation in diffraction efficiency into the +1st diffraction order at and away from the resonant wavelength. On resonance the device operates with a diffracted efficiency of 60%.
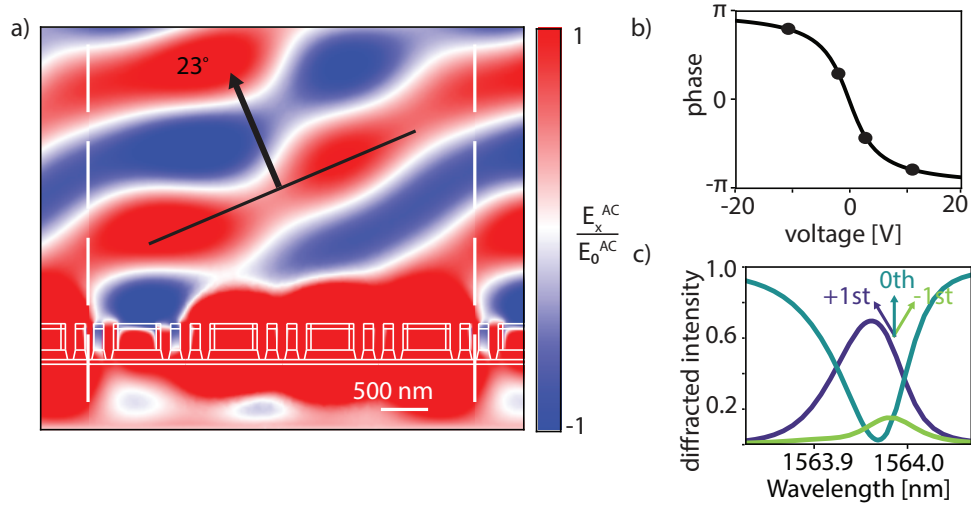
Figure 10: Electro-optically reconfigurable metasurface beamsteerer with four bars in the supercell. (a) Visualization of beamsteering at 1563.96 nm when the series of four voltages are applied to the metasurface; white dotted lines denote the supercell period. (b) Phase delay dictated by applied voltage without accounting for residual coupling between bars, four voltages (-11.2, -1.9, +1.9, +11.2 V) are selected (black markers) to achieve a $2\pi/4$ phase change between them. (c) Variation in diffraction efficiency into the +1st diffraction order at and away from the resonant wavelength. On resonance the device operates with a diffracted efficiency of 70%.
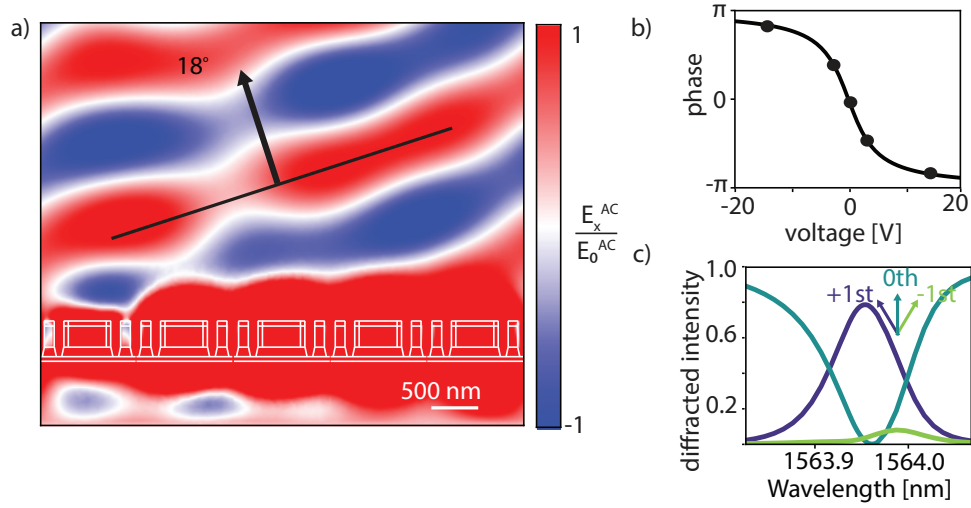
Figure 11: Electro-optically reconfigurable metasurface beamsteerer with five bars in the supercell. (a) Visualization of beamsteering at 1563.96 nm when the series of five voltages are applied to the metasurface; white dotted lines denote the supercell period. (b) Phase delay dictated by applied voltage without accounting for residual coupling between bars, five voltages (-14.3, -3.4, 0, +3.4, +14.3 V) are selected (black markers) to achieve a $2\pi/5$ phase change between them. (c) Variation in diffraction efficiency into the +1st diffraction order at and away from the resonant wavelength. On resonance the device operates with a diffracted efficiency of 80%.

Accounting for residual coupling for highest efficiency beamsplitting and beamsteering

Although the optically isolating fins allow for individual tuning of neighboring antennas, some coupling will remain in our system. Applying a voltage to perturb resonances in individual bars, this results in a broadening of the resonance. This causes the associated phase response to also broaden with respect to applied voltage. This broadening depends on the phase difference between bars, and we take this coupling into account when calculating the voltages required to tune the phase response of the nanoantennas to achieve the desired transfer function.

When designing our maximum efficiency beamsplitting and beamsteering devices, we account for the coupling between bars that results in the broadening of the phase response from applied voltage by sweeping the applied voltage(s) on the various nanoantennas in the supercell at the design wavelength of 1563.96 nm to maximize the diffracted efficiency to the desired diffraction order. For the beamsplitter formed by applying two biases, this results in a maximized combined ±1st order efficiency of 93% by applying voltages of ±11.3 V between neighboring bars (fig. S12a). Similarly, for a beamsteerer formed by applying three biases, a maximized +1st diffraction efficiency of 76% is achieved for applied voltages of ±14.5 V and 0 V (fig S12b). For beamsteerers of larger supercells, multiple sets of voltages must be swept simultaneously. For a beamsteerer formed by applying four biases, a maximized +1st diffraction efficiency of 80% is achieved for applied voltages of ±18.6 V and ±2.7 (fig S12c). For a beamsteerer formed by applying five biases, a maximized +1st diffraction efficiency of 86% is achieved for applied voltages of ±21.1 V, ±5, and 0 V (fig S12d). Finally, the curve that defines the relationship between applied voltage and resulting nanoantenna phase response can be adjusted according to the broadening associated with coupling in the case for each supercell (fig S12e).

Interestingly, beamsplitting behavior improves slightly off resonance at 1563.99 nm,
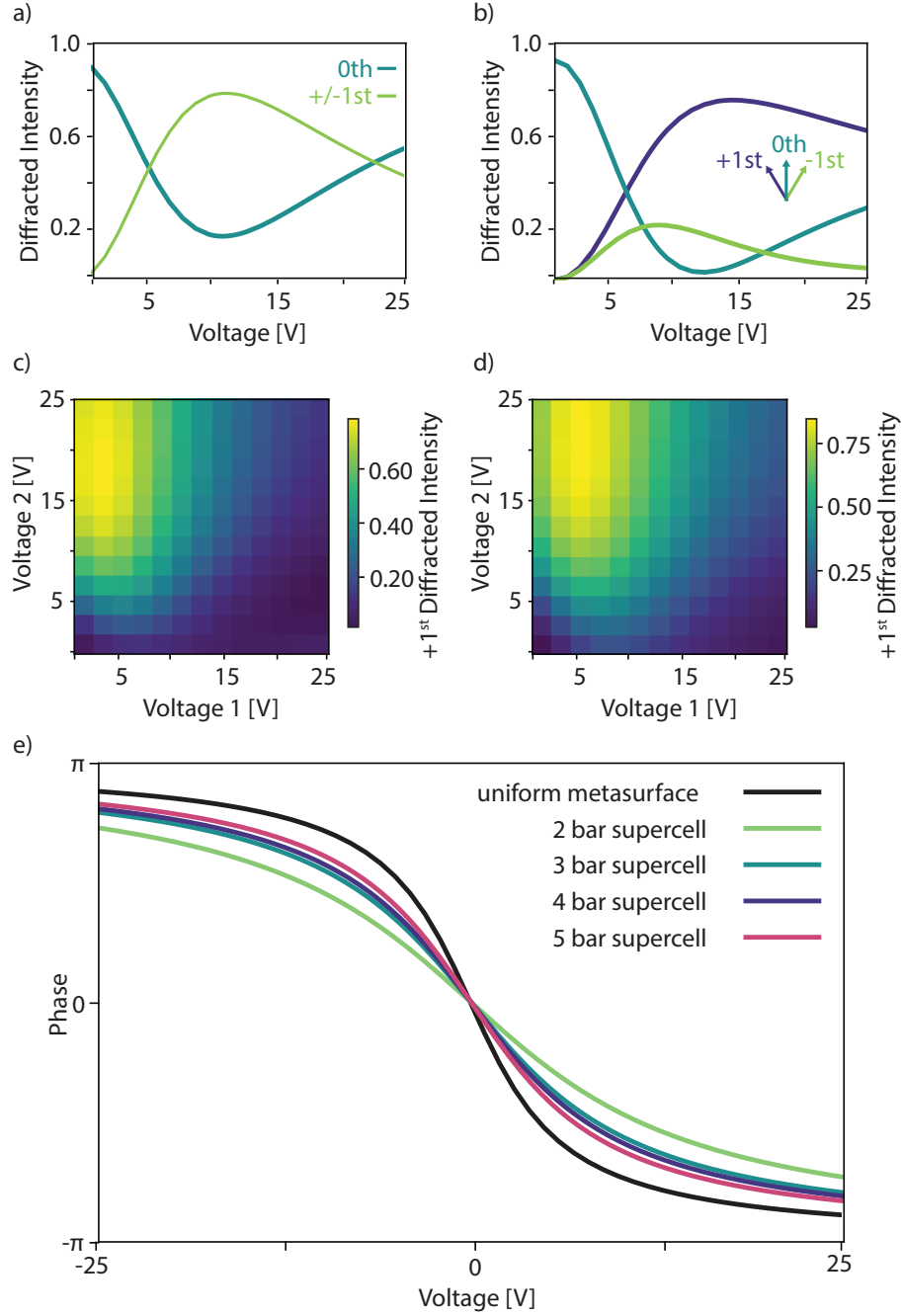
Figure 12: Diffracted intensity at 1563.96 nm with respect to voltage applied for a (a) 2 bar supercell with applied voltages of $\pm$V, (b) 3 bar supercell with applied voltages of +V, 0 V, and -V, (c) 4 bar supercell with applied voltages of +Voltage 2, +Voltage 1, -Voltage 1, -Voltage 2, and (d) 5 bar supercell with applied voltages of +Voltage 2, +Voltage 1, 0 V, -Voltage 1, -Voltage 2. (e) Broadening of the phase response with applied voltage modeled for different supercell sizes, resulting from varying amounts of coupling in each case.

achieving a maximum combined $\pm$1st order efficiency of 96% for applied voltages of $\pm$14.3 V (fig. S13a). This could be accounted for by the increase in overall reflected light from 91% at 1563.96 nm to 98% at 1563.99 nm. Figure S13b shows the reflected spectra when $\pm$14.3 V are applied to the metasurface, and figure S13c shows the reflected field at 1563.99 nm with $\pm$14.3 V applied. The beamsteering metasurfaces do not show this behavior.
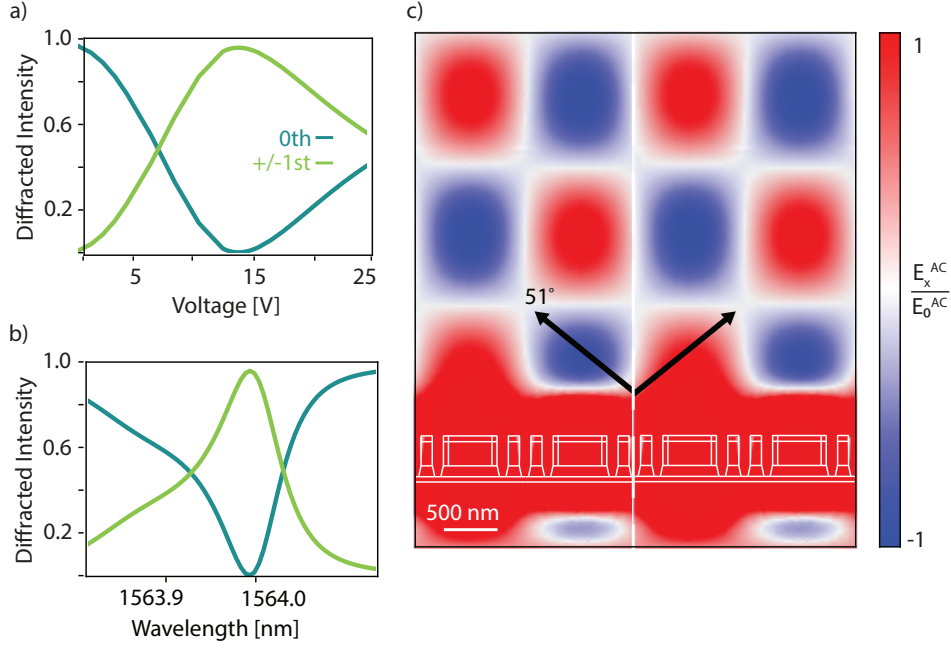

Figure 13: (a) Diffracted intensity with respect to applied voltage for a 2 bar supercell at 1563.99 nm. (b) Spectra across the resonance with applied voltages of $\pm$14.3 V. (c) Visualization of beamsteering with the applied voltages at 1563.99 nm.

Furthermore, as discussed previously, coupling is exacerbated without the inclusion of nanofins in the system. As such the same applied voltage sweeps are necessary to define the most optimized case for these metasurfaces that experience these coupling effects as well. For the beamsplitter achieved with a 2 bar supercell, this results in a maximized combined $\pm$1st order efficiency of 49% by applying voltages of $\pm$21 V between neighboring bars (fig. S14a). Similarly, for a beamsteerer achieved with a 3 bar supercell, a maximized +1st diffraction efficiency of 23% is achieved for applied voltages of $\pm$23 V and 0 V (fig S14b),

with 19% efficiency into the -1st diffraction order. Further details on these metasurfaces, including phase response for the supercell, corresponding reflection in the various diffraction orders across the resonance, and visualization of the resulting field and diffraction angle(s) are found in the main text (fig 3b-d) and below (fig S15).
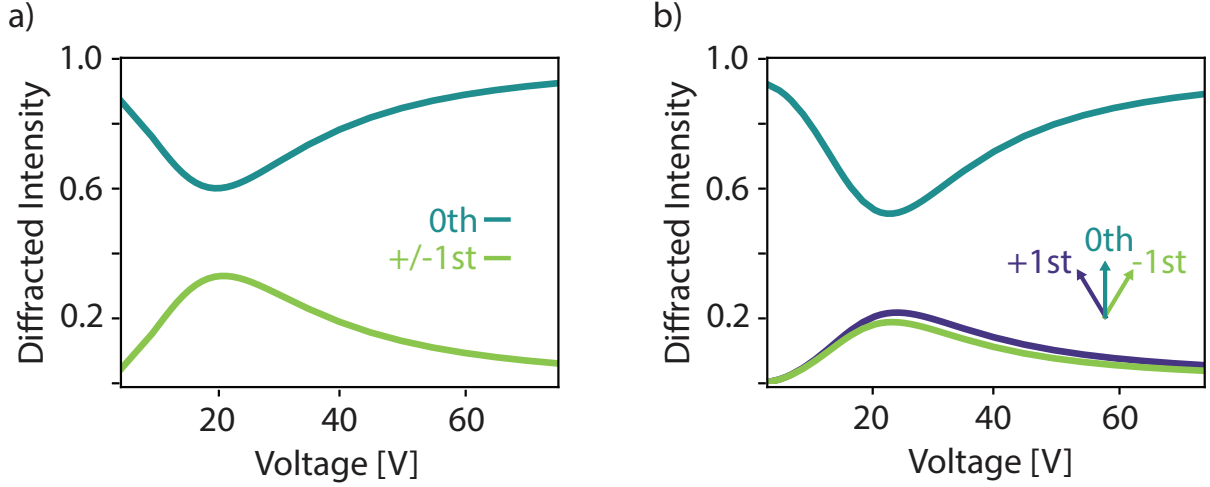

Figure 14: Diffracted intensity from a metasurface with no fins between the antennas with respect to applied voltage at 1560.65 nm for a (a) 2 bar supercell and (b) 3 bar supercell.

Extraneous diffraction orders for tunable beamsteerers

Larger metasurface supercells support diffraction orders beyond the ±1st. When diffraction is maximized in the +1st order at 1563.96 nm, the 4 bar supercell beamsteerer sends less than 5% of light to the combined ±2nd order diffraction (fig S16a) and the 5 bar supercell beamsteerer sends less than 5% of light to the ±2nd and 3rd order diffraction (fig S16b). As such, we consider these extraneous diffraction orders negligible in our system.
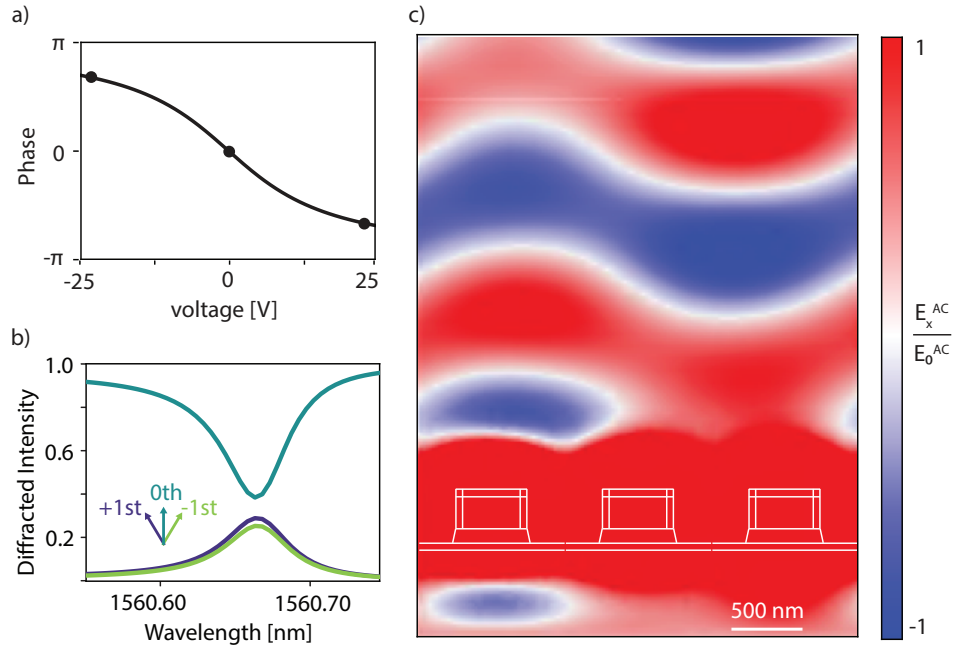
Figure 15: (a) Phase delay dictated by applied voltage on a metasurface without fins between the antennas, three voltages (-23 V, 0 V, +23 V) are selected (black markers) to achieve a $2\pi/3$ phase change between them. (b) Variation in diffraction efficiency at and away from the resonant wavelength. (c) Visualization of the field at 1560.65 nm when the series of three voltages are applied to the metasurface.
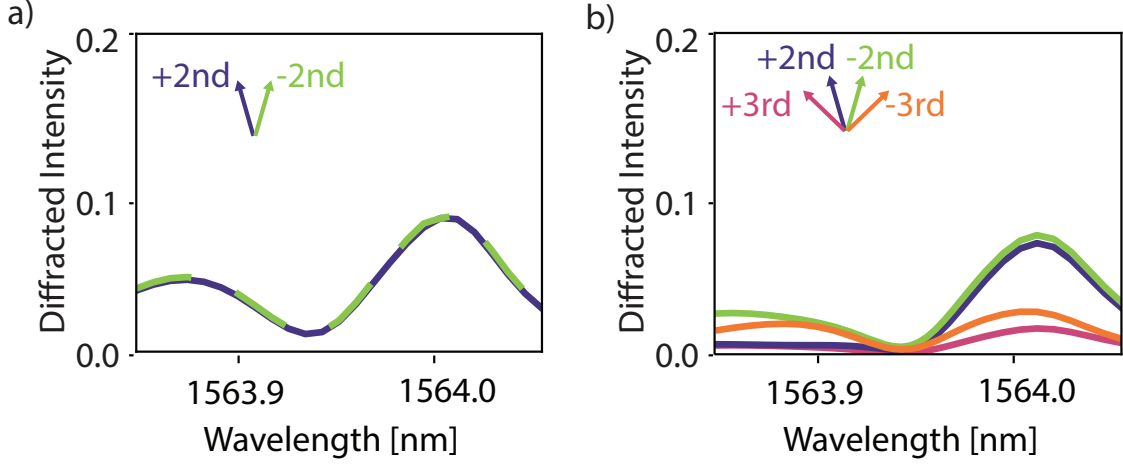
17

Figure 16: (a) Diffraction efficiency into the ±2nd diffraction orders at and away from the resonant wavelength for the tunable beamsteerer reported in Figure 4e-g. (b) Diffraction efficiency into the ±2nd and ±3rd diffraction orders at and away from the resonant wavelength for the tunable beamsteerer reported in Figure 4h-j.

Pixelating metasurfaces for continuous angle beamsteering

Pixelating metasurfaces on a single chip can further enhance the functionality of our tunable metasurface-based devices. In a single metasurface, the number of voltages applied, and thus the number of bars in a supercell period, determine the beamsteering angle. The possible beamsteering angles are determined by the unit cell dimensions of the metasurface. When metasurfaces are pixelated, adjacent pixels can have different unit cell widths resulting from tuning the bar width or spacing to achieve the desired dimensions. This allows each metasurface pixel to access a different set of beamsteering angles, shown in figure S17, enabling near-continuous beamsteering in a single metasurface-based device.
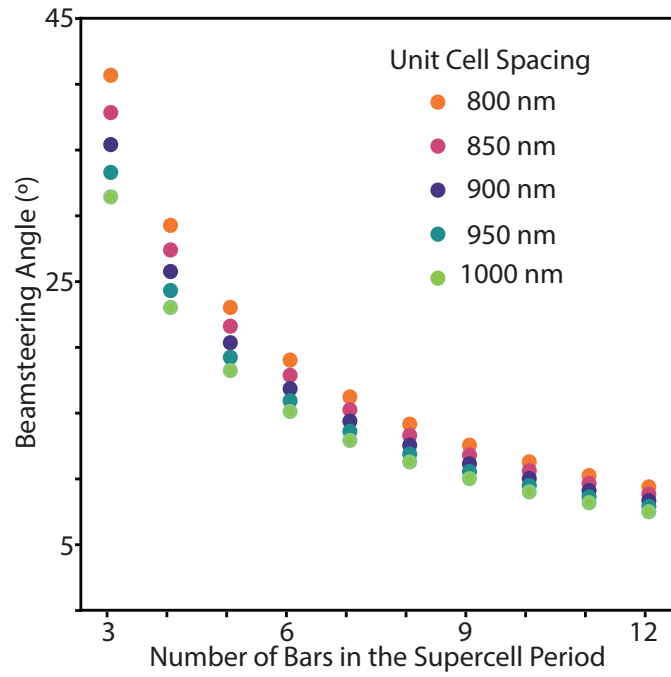
Figure 17: Achievable diffractive beamsteering angles based on geometric constraints of the metasurface platform. Inclusion of multiple metasurfaces onto a single device could thus enable more continuous beamsteering.

Effect of possible losses introduced by fabrication

As this work only explores the theoretical design and function of this platform, we generally do not consider the possible losses of the materials involved. While silicon and lithium niobate are dielectrics and do not demonstrate strong losses in the near infrared regime, realizing this platform experimentally will necessarily involve fabrication imperfections and the introductions of losses. For instance, surface roughness can be introduced. Prior work in the literature generally shows high-Qs are feasible in silicon and lithium niobate structures separately,[1–3] but surface roughness that may be introduced from fabricating the proposed layered structure may affect the potential Q factor that is able to be achieved in this structure.

Here we consider these possible surface losses by simulating a 10 nm region of the LNO near its bare edges with varying imaginary components of the refractive index (k). As shown in Figure S18b, the introduction of loss affects the reflectance across the resonance strongly. This could impact the maximum potential device efficiency. More importantly, however, the phase variation across the resonance is well preserved at many possible k values. This is likely because the high-Q field is well contained between the Si and LNO, and would not be as strongly perturbed by surface effects.

To move to a fully experimental design, many features of the current device may need further optimization, as we cannot take into account all possible conditions of fabrication. However, this study supports the core mechanism that underpins our novel approach to dynamic metasurfaces.
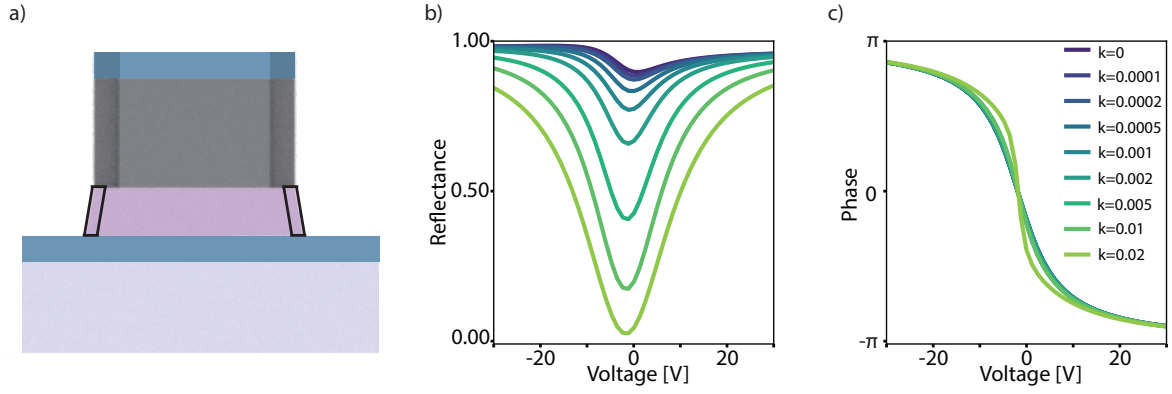
Figure 18: a) Region of surface losses modeled at a 10 nm region b) Spectra of resonant metasurface showing reflectance varying with increasing k (or the imaginary component of the refractive index) c) Phase variation across the resonance for various k values.

References

(1) Zhang, M.; Wang, C.; Cheng, R.; Shams-Ansari, A.; Lončar, M. Monolithic ultra-high-Q lithium niobate microring resonator. *Optica* **2017**, *4*, 1536.

(2) Wang, J.; Bo, F.; Wan, S.; Li, W.; Gao, F.; Li, J.; Zhang, G.; Xu, J. High-Q lithium niobate microdisk resonators on a chip for efficient electro-optic modulation. *Optics Express* **2015**, *23*, 23072.

(3) Li, M.; Ling, J.; He, Y.; Javid, U. A.; Xue, S.; Lin, Q. Lithium niobate photonic-crystal electro-optic modulator. *Nature Communications* **2020**, *11*, 4123.